Plasmon-induced optical magnetism in an ultrathin metal nanocavity

Yongjun Meng[1,2,#], Qiang Zhang[3,4,5,#], Dangyuan Lei[6,#], Yonglong Li[7], Siqi Li[1], Xiaolin Chen[6], Zhenzhen Liu[5], Wei Xie[7], Chi Wah Leung[1]

Abstract

Recently, plasmon-induced optical magnetism has appealed much research interest in nanophotonics and plasmonics due to intriguing applications potentially in optical metamaterials, ultrasensitive plasmonic nano-metrology, enhanced nonlinear harmonic generation and so on. To the best of our knowledge, here we for the first time experimentally and theoretically observe a strong in-plane magnetic dipolar resonance in an ultrathin plasmonic nanocavity consisting of a silica-coated gold nanosphere dimer coupled to a gold thin film. Combining multipolar expansions and full-wave numerical simulations, we reveal that the magnetic resonance is induced by a displacement current loop circulating around the nanometer thick triangular region enclosed by the sphere dimer and the gold film, leading to drastically enhanced magnetic field intensity in the cavity gap. Using polarization-resolved dark-field imaging and spectroscopy at the single-particle level, we unambiguously "visualize" the spectral response and radiation polarization of the induced magnetic mode, exhibiting features quite different from electric dipolar resonances. We further find that the magnetic resonance frequency highly depends on both cavity gap thickness and nanosphere dimension, allowing a straightforward resonance tuning from the visible to the near-infrared region and thus opening up a new avenue for magnetic resonance enhanced nonlinear optics and chiral optics.

Introduction

Sub-wavelength artificial structures supporting pronounced magnetic resonance, referred as magnetic meta-atoms or meta-molecules, are crucial elements for constructing negative-index metamaterials[1-3] and versatile metasurfaces[4-6]. A classical paradigm of such meta-atoms is the split ring resonator adopted in the microwave range[7-9]. In general, the magnetic resonance frequency of a split ring resonator saturates at optical frequencies upon scaling down its size because the conduction property of metals in the near-infrared and visible spectral regions is distinctively different from that in the microwave and infrared regions[10,11]. To realize artificial optical magnetism at higher frequencies, several elegant scenarios were proposed[12,13]. For example, high-index dielectric nanoparticles can sustain magnetic resonances due to the induced displacement current loops under the visible light excitation[14-17]. Different from high-index dielectric nanoparticles that support both electric and magnetic multipolar Mie resonances, the optical responses of metallic nanoparticles are dominated by the localized surface plasmon resonance (LSPR) that inherently bears the electric resonant nature[18,19]. Nevertheless, hybridized plasmon modes in coupled metallic nanoparticle clusters are demonstrated to exhibit pronounced magnetic responses when the induced electric dipoles in the cluster are arranged head-to-tail in a loop configuration[20-29].

In 2010, Fan et al. attained an optical magnetic resonance in a self-assembled gold nanosphere planar trimer, with the induced magnetic response severely overwhelmed by the electric one[20]. The presence of such magnetic resonances allows for significant destructive interference with the electric resonances so as to generate pronounced Fano resonances when the symmetry of the planar cluster is broken[21,22,24]. The first observation of the magnetic-based optical Fano resonance was reported by Shafiei et al. in 2013 in a four-particle

Correspondence: Dangyuan Lei (dangylei@cityu.edu.hk)

[1]Department of Applied Physics, The Hong Kong Polytechnic University, Hong Kong 999077, China

[2]School of Physics, Huazhong University of Science and Technology, Wuhan, Hubei, China

[3]Department of Physics and Optoelectronics, Taiyuan University of Technology, Taiyuan 030024, China

[4]Key Lab of Advanced Transducers and Intelligent Control System of Ministry of Education, Taiyuan University of Technology, Taiyuan 030024, China

[5]Shenzhen Engineering Laboratory of Aerospace Detection and Imaging, College of Electronic and Information Engineering, Harbin Institute of Technology (Shenzhen), Shenzhen 518055, China

[6]Department of Materials Science and Engineering, City University of Hong Kong, Hong Kong 999077, China

[7]Key Lab of Advanced Energy Materials Chemistry (Ministry of Education), Renewable Energy Conversion and Storage Center, College of Chemistry, Nankai University, Tianjin 300071, China

nanoring prepared by atomic force microscope nano-manipulation[21]. Large areas of plasmonic nanoclusters composed of nanoparticles with flat surfaces such as nanodisks and nanopatches were fabricated by top-down methods including electron beam lithography and focused ion beam[25-27]. However, the minimum inter-particle distances in those metallic nanoclusters are limited typically to about 10 nm, hindering extreme magnetic field confinement and enhancement.

In addition to the above-mentioned metal nanoparticle clusters, plasmonic particle-on-film nanocavities (PoFNs) formed by closely spaced metal nanoparticles and a metal film were also demonstrated as a feasible platform to generate plasmon-induced magnetic resonances[30-33]. In physics, the plasmon responses of such PoFNs can be simply understood by an anti-phase hybridization between the plasmon modes of the real particles and the counterparts of their images in the metal film[34]. From this point of view, PoFNs can be considered as a peculiar form of plasmonic nanoclusters. But it is worth noting that the induced magnetic dipole moments in such PoFNs are parallel to the substrate supporting the particles, rather than perpendicular to the substrate as in the case of planar nanoparticle clusters. Most studies on plasmon-induced magnetic resonances in the PoFNs adopt metal nanoparticles with flat surfaces, leading to relatively large mode volumes and hence loosening the near-field confinement. For example, the magnetic resonances in metallic disk-on-film and cube-on-film nanocavities have been widely applied in designing metamaterial absorbers in the infrared and visible ranges[30-32].

For a plasmonic PoFN constructed by a single metal nanoparticle of spherical shape coupled to a metal film, such as a nanosphere monomer-on-film nanocavity (MoFN), its optical response is usually dominated by an electric resonance[34-39]. Recently, Chen et al. showed that an optical magnetic resonance can also be realized in a nanosphere MoFN, provided that the diameter of the nanosphere is large enough[40]. The magnetic resonance in such a nanosphere MoFN is produced essentially by the displacement current loop that is tightly squeezed in the nanometer-thick particle-film gap. This work indicates that for even the simplest nanosphere MoFN system, near-field coupling between the particle and the metal film is capable of producing rich plasmon modes of both electric and magnetic characteristics. Naturally, it is expected that complex nanosphere-based PoFN configurations with multiple bounded metal nanospheres support more versatile plasmon modes, benefiting from the co-existence of particle-particle and particle-film couplings. However, studies on nanosphere PoFNs consisting of multiple coupled spherical nanoparticles remain relatively rare, probably due to the difficulties in precision construction. In fact, two previous theoretical and numerical studies on nanosphere dimer-on-film nanocavities (DoFNs) showed that, under normal incidence, the horizontally polarized bonding modes of the dimer couple to the metal film, resulting in multiple distinctive film-coupled bonding modes[41,42], including a dipole-quadruple hybridized resonance and a magnetic resonance (though both studies failed to point out the latter).

Our earlier experimental observations confirmed the presence of the dipole-quadruple hybridized resonance in the plasmonic nanosphere DoFN system through distinguishing its scattering spectrum and radiation pattern from pure bonding dipolar resonances[35,43,44]. However, so far the plasmon-induced optical magnetic resonance predicted for the nanosphere DoFN system remains unexplored in experiment. Here we for the first time present the experimental observation of a magnetic resonance in a gold nanosphere DoFN system under normal incidence. In addition, we combine multipolar expansions and numerical full-wave simulations to unambiguously reveal its accurate physical origin, and perform comprehensive single-particle dark-field imaging and scattering spectroscopy to disclose its geometry dependence and radiation properties.

Results

With the aid of full-wave electromagnetic simulations, we first determine the plasmon resonance modes in a gold nanosphere DoFN under excitation by a linearly polarized plane wave. Without loss of generality, here we consider the nanosphere DoFN formed by two identical gold nanospheres (100 nm diameter) coated with 1.5 nm of SiO_2, which are in contact with one another and coupled to a gold thin film. This leads to a 3-nm particle-particle gap distance and a 1.5 nm particle-film gap distance. For a comprehensive understanding of the plasmon modes supported by the nanosphere DoFN system, we numerically

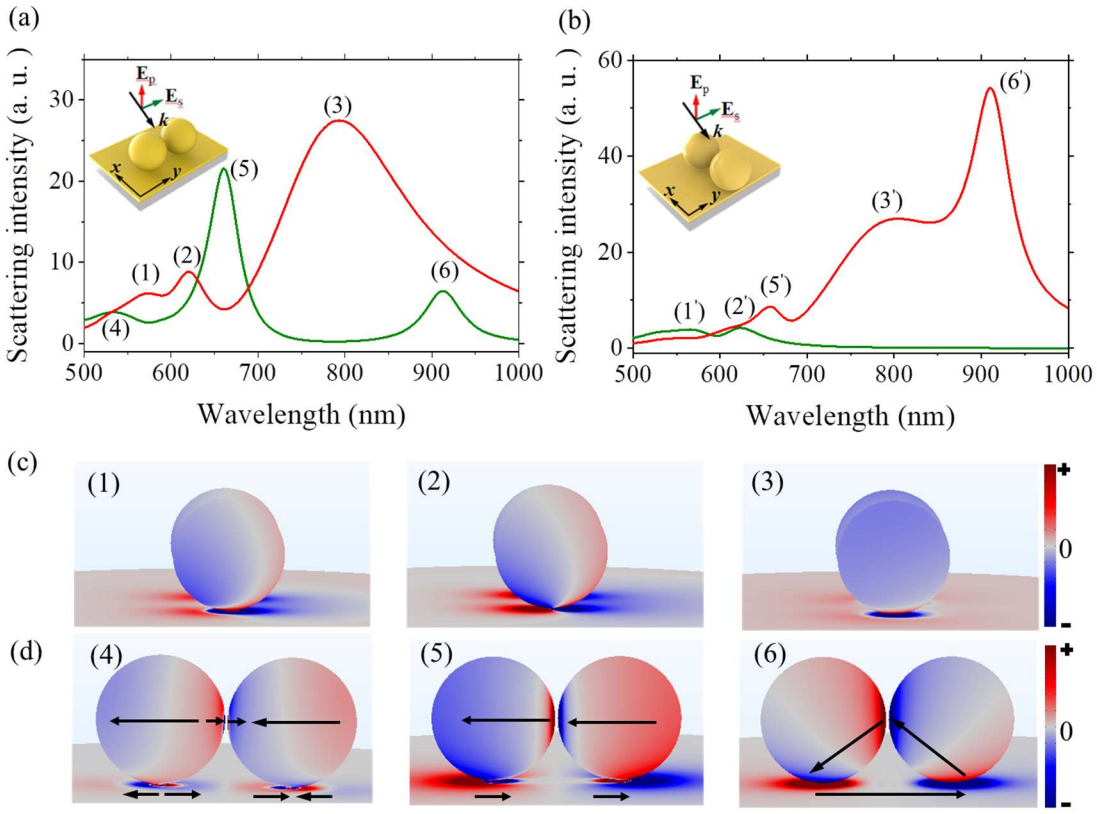

Fig. 1 Numerical investigation of the plasmonic responses of nanosphere DoFN excited by linearly polarized plane waves with incidence angle of 70°. a s-polarized (olive line) and p-polarized (red line) scattering spectra of the nanosphere DoFN in excitation configuration (I) where the long axis of the dimer is perpendicular to the incidence direction. **b** Similar to **a** but in excitation configuration (II) where the long axis of the dimer is nearly parallel to the incidence direction. Insets in **a** and **b** are the schematics of the nanosphere DoFNs and the corresponding excitation configurations. Different plasmon modes are labeled by the numbers in brackets near the corresponding scattering peaks on the spectra. **c** Snapshots of the transient surface charge distributions of transversely hybridized horizontal electric modes [(1) and (2)] and vertical electric mode (3). **d** Snapshots of the transient surface charge distributions of film-coupled longitudinal bonding modes [(4), (5), and (6)]. Black arrows in **d** represent the induced transient electric dipoles.

calculate its scattering spectra under oblique incidence with a horizontal polarization either parallel or perpendicular to the dimer axis. Because the nanosphere DoFN has a C_2 rotation symmetry, two excitation configurations are considered, where the long axis of the dimer is perpendicular or nearly parallel to the incidence direction (represented by the wavevector $\boldsymbol{k}$) (referred as configuration (I) and configuration (II), respectively). In each configuration, the incident plane wave is either s- or p-polarized as depicted in the insets in Fig. 1.

Fig. 1a shows the calculated p-polarized (red line) and s-polarized (olive line) scattering spectra in excitation configuration (I). We notice that the p-polarized scattering spectrum is quite similar to that of a nanosphere MoFN under the same excitation configuration as we previously reported[35]. If we consider the nanosphere DoFN as two coupled MoFNs, the predominant scattering peaks [labeled as (1) at 570 nm, (2) at 620 nm and (3) at 790 nm] in the p-polarized scattering spectrum (red line) can be attributed to hybridized modes formed by the coupling between two nanosphere MoFNs. As the polarization direction is perpendicular to long axis of the dimer, the coupling is transverse and is relatively weak, which leads to scattering responses similar to that of single nanosphere MoFN.

To identify these resonances, we plot in Fig. 1c the snapshots of the transient surface charge distributions of modes (1), (2) and (3), respectively. For both modes (1) and (2), the opposite surface charges on each particle and on the metal film are separated along the horizontal direction, although the nodal lines of the neutral charges are somehow distorted due to the presence of vertical electric field component of the excitation. Thus we confirm that modes (1) and (2) correspond to the transversely hybridized horizontal electric modes

excited by the electric field component parallel to the metal film. The only difference between modes (1) and (2) is that the former has additional nodal lines of neutral charges, which indicates that mode (1) corresponds to a higher order mode.

Regarding the mode (3), it can be attributed to a transversely hybridized vertical electric dipolar mode, which is characterized by the opposite surface charges on each particle separated along the direction normal to the metal film. Due to the predominantly out-of-plane electric field component of the excitation and the significant particle-film coupling, mode (3) has a very large vertical electric dipole moment that contributes to the strong scattering intensity.

When the polarization is parallel to the dimer's long axis (i.e. s-polarized), the longitudinal coupling between two monomer cavities is so strong that the optical responses of the nanosphere DoFN exhibit quite different features. This is confirmed by the s-polarized scattering spectrum of the nanosphere DoFN in Fig. 1a (olive line), where three new plasmon modes show up and contribute to the scattering peaks on the spectrum (labeled as (4) at 530 nm, (5) at 660 nm and (6) at 912 nm). The induced surface charges of all these three modes are anti-symmetric with respect to the vertical axis of the nanosphere DoFN (Fig. 1d). Based on this observation, we argue that these three modes originate from the coupling between the longitudinal bonding plasmon modes sustained by the dimer and the corresponding mirrored modes induced in the metal film (which corresponds to the film-coupled bonding modes as termed in previous studies)[41].

Yet, the induced transient electric dipoles as denoted by the black arrows in Fig. 1d indicate they have different resonant features. For modes (4) and (5), the transient electric dipole moments in the dimer are nearly parallel to the metal film. Moreover, surface charges at the bottom of each particle induce electric dipoles in the metal film under the particle-film gaps. Compared to mode (5), mode (4) belongs to a higher order mode as characterized by more nodes of neutral charges and electric dipoles. This is in sharp contrast with mode (6), which shows dramatically different resonant features with respect to modes (4) and (5), with the dimer as a whole induces a single electric dipole in the metal film. More importantly, the three electric dipoles in the cavity form a triangular loop in a head-tail fashion due to the strong bonding interaction among them. Based on this distinctive feature, we speculate that the mode (6) actually corresponds to a plasmon-induced magnetic resonance which is the key finding of this work as to be discussed in details later.

By rotating the dimer in Fig. 1a by 90°, the excitation is changed to configuration (II) and the scattering spectra is significantly changed (Fig. 1b). In this excitation configuration, the s-polarized spectrum (olive line) is almost identical to that of a SMoFN, which shows only two scattering peaks at the same wavelengths as modes (1) and (2) in Fig. 1a. These two modes are transversely hybridized horizontal electric modes of the nanosphere DoFN. Here, however, we label them as modes (1') mode (2') considering several different features compared to modes (1) and (2). First, the induced dipoles in the particles are parallel to the metal film plane in modes (1') and (2'), since the s-polarized wave in excitation configuration (II) only has in-plane electric field component that is orthogonal to the dimer. Second, the symmetry of the two particles with respect to the $\boldsymbol{k}$-vector of the incident wave is broken, resulting in phase differences between particles (Fig. S1a). In contrast, the in-plane electric field component of the p-polarized wave now becomes parallel to the long axis of the dimer (inset in Fig. 1b), which means the film-coupled longitudinal bonding modes can be excited.

Meanwhile, the predominantly out-of-plane electric field component of the excitation also evokes the strong transversely-hybridized vertical electric dipole mode. Due to the large radiation loss, this vertical electric dipole mode has much broader linewidth than other film-coupled longitudinal bonding modes. As a result, all the scattering peaks from the film-coupled bonding modes sit on the shoulder of the wide scattering peak of the vertical electric dipole mode, as seen in the p-polarized spectrum (red line) in Fig. 1b. Similarly, to distinct these modes to those excited in configuration (I) (Fig. 1a), we label them as modes (5'), (3') and (6') from short to long wavelength in the p-polarized scattering spectrum in Fig. 1b. The transient surface charge distributions (Fig. S1b) of modes (5'), (3') and (6') have features of both the film-coupled modes and the vertical electric dipole mode. Arguably, mode (4') should also be excited by the p-polarized

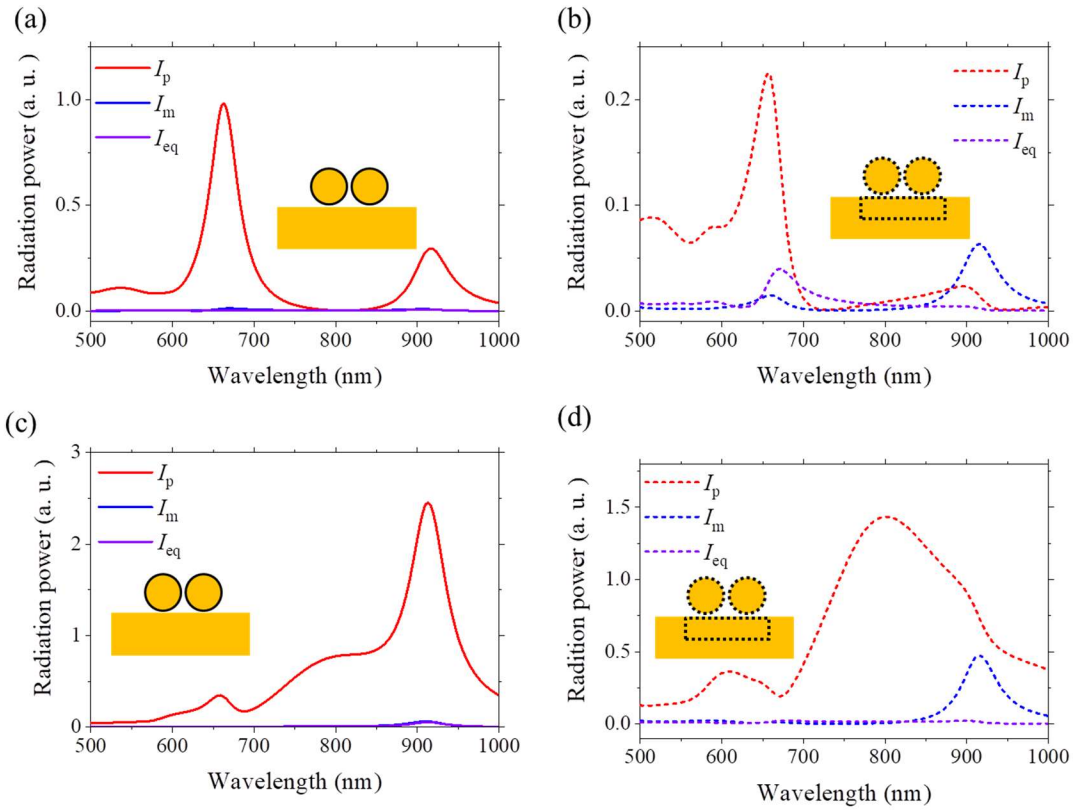

Fig. 2 Multipole decomposition of the radiation power of the nanosphere DoFN. a Radiation power from the electric dipole (red line), magnetic dipole (blue line), and electric quadrupole (violet line) of the nanosphere DoFN excited by the s-polarized plane wave in configuration (I). Here, the multipole moments are obtained by only considering the contribution from the dimer itself, i.e. the domains enclosed by the black line in the inset. **b** Similar to **a**, but the multiple moments are obtained by considering both the dimer and the nearby metal film, i.e. the domains enclosed by the black dashed lines in the inset. **c** and **d** are similar to **a** and **b**, respectively, but the nanosphere DoFN is excited by the p-polarized plane wave in configuration.

plane wave in configuration (II), but it is difficult to discern it on the scattering spectrum due to its weak excitation strength. Here we stress that mode (6') essentially holds the same magnetic resonant nature as mode (6), although it is mixed with the vertical electric mode (3).

In the above discussions, we demonstrated that different plasmon modes of a nanosphere DoFN can be distinguished by inspecting its polarization-resolved far-field scattering spectra. In particular, we preliminarily point out that the nanosphere DoFN supports a plasmon-induced magnetic resonance which can be excited when the magnetic field of the incident wave has flux across the triangular region formed by the dimer and the metal film. To further verify this conclusion, we use the multipole expansion to identify the plasmon multipole modes observed in Fig. 1. The multipole moments in Cartesian coordinate system are determined by the distributions of the polarization current $\mathbf{J}(\mathbf{r}')=-i\omega\varepsilon_0(\varepsilon_r-1)\mathbf{E}(\mathbf{r}')$ induced in the nanoparticles, where $\mathbf{r}'$ is the position vector with respect to the mass center of the particles, ω is the angular frequency, ε_0 is the permittivity of the vacuum, ε_r is the relative permittivity of the nanoparticles, $\mathbf{E}(\mathbf{r}')$ is the electric field inside the nanoparticles, and $i=\sqrt{-1}$. Here, we only consider the first three predominant multipoles in the nanosphere DoFN, i.e. electric dipole, magnetic dipole and electric quadrupole. The corresponding electric dipole moment $\mathbf{P}$, the magnetic dipole moment $\mathbf{M}$, and the electric quadrupole tensor $\hat{Q}^e$ can be calculated by the following Eqs. (1)-(3):

$$\mathbf{P}=-\frac{1}{i\omega}\int\mathbf{J}(\mathbf{r}')d^3\mathbf{r}', \tag{1}$$

$$\mathbf{M}=\frac{1}{2c}\int\mathbf{r}'\times\mathbf{J}(\mathbf{r}')d^3\mathbf{r}', \tag{2}$$

$$\hat{Q}^e=-\frac{1}{i\omega}\int\left[\mathbf{r}'\mathbf{J}(\mathbf{r}')+\mathbf{J}(\mathbf{r}')\mathbf{r}'-\frac{2}{3}\hat{\mathbf{I}}[\mathbf{r}\cdot\mathbf{J}(\mathbf{r}')]\right]d^3\mathbf{r}', \tag{3}$$

where $\hat{\mathbf{I}}$ in Eq. (3) is a 3×3 unit tensor. The time-average radiation powers from electric dipole (I_p), magnetic dipole (I_m), and electric quadrupole (I_{eq}) in vacuum are given as follows:

$$I_{\mathrm{p}} = \frac{\omega^4 |\mathbf{P}|^2}{12\pi c^3 \varepsilon_0}, \tag{4}$$

$$I_{\mathrm{m}} = \frac{\omega^4 |\mathbf{M}|^2}{12\pi c^3 \varepsilon_0}, \tag{5}$$

$$I_{\mathrm{eq}} = \frac{\omega^6 \left|\hat{Q}^e\right|^2}{160\pi c^5 \varepsilon_0}, \tag{6}$$

where c is the speed of light in vacuum[44-47]. It should be noted that a rigorous multipole decomposition of radiation powers of nanoparticles placed on a metal substrate needs to consider the contributions from the reflected waves by the film. This means that Eqs. (4)-(6) must be modified due to the different dyadic Green's functions responsible for the waves directly radiated from the particles and the waves reflected by the substrate. For simplicity, here we apply Eqs. (4)-(6) to calculate the radiation powers from the multipoles, but their moments are obtained from Eqs. (1)-(3) by integrating the polarization currents only in the dimer itself or in both the dimer and the nearby gold film. This treatment of multipole decomposition is adequate for qualitative identification of the multipolar modes in the nanosphere DoFN.

Figure 2 shows the results of the multipolar expanded radiation power of the nanosphere DoFN excited by the s- (p-) polarized linearly plane wave in configuration (I) (configuration (II)). It is seen that the radiation power from electric dipole (red lines) dominates over the whole spectral range (500 - 1000 nm) in Fig. 2a and Fig. 2c, when only the polarization current in the dimer itself is considered. However, when the gold film close to the dimer is also included in the integration domains in Eqs. (1)-(3) (Fig. 2b and Fig. 2d), significant resonant peaks of the radiation power from magnetic dipole (blue lines) show up at the wavelength of 912 nm. Particularly, Fig. 2b shows that the radiation power from magnetic dipole can be much larger than that from electric dipole and electric quadrupole when the incidence polarization is parallel to the dimer's long axis, which further confirms that mode (6) is a magnetic dipolar mode. More importantly, the absence of magnetic dipole in Figs. 2a and 2c implies that the induced current in the metal film close to the dimer is crucial for generating the magnetic dipolar mode.

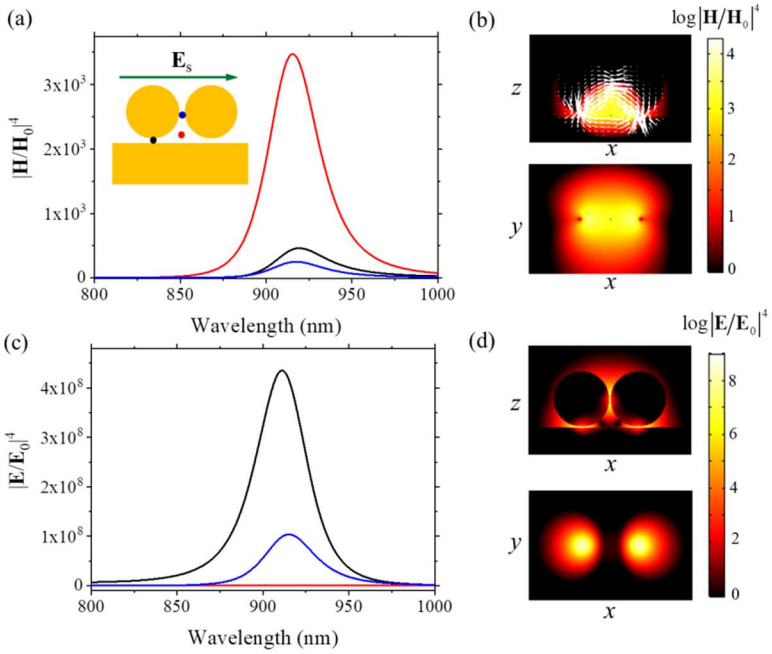

Fig. 3 Near field properties of the magnetic resonance mode (6). a Spectra of the magnetic near-field enhancement factor $|\mathbf{H}/\mathbf{H}_0|^4$ monitored at three key locations in the nanosphere DoFN excited by the s-polarized plane wave in configuration (I). The key locations are denoted by black, red, and blue dots in the inset. **b** $|\mathbf{H}/\mathbf{H}_0|^4$ distributions of the magnetic mode (6) in xz-plane (top) and xy-plane (bottom), respectively. **c** Spectra of the electric near-field enhancement factor $|\mathbf{E}/\mathbf{E}_0|^4$ monitored at the same points as in **a**. **d** $|\mathbf{E}/\mathbf{E}_0|^4$ distributions of the magnetic mode (6) in xz-plane (top) and xy-plane (bottom), respectively.

Next, we discuss the near-field properties of the pure magnetic dipolar mode (6). Fig. 3a shows the spectra of the magnetic near-field enhancement factor $|\mathbf{H}/\mathbf{H}_0|^4$ monitored at three key locations in the structure (black, red, and blue dots in the inset) in the wavelength range of 800 to 1000 nm. Here, $\mathbf{H}$ is the total magnetic field of the nanosphere DoFN and $\mathbf{H}_0$ is the magnetic field of the incident plane wave. It shows that all the spectra show Lorentz profiles with the same resonant wavelength as that of mode (6) obtained from the far-field scattering spectrum (olive line in Fig. 1a). Moreover, the peak strength of $|\mathbf{H}/\mathbf{H}_0|^4$ (red line) near the center of the triangular region formed by the dimer and the metal film (red dot) is much larger than those (black and blue lines) at the contact points between particle-film (black dot) and the particle-particle (red dot) gaps.

Correspondingly, Fig. 3b plots the $|\mathbf{H}/\mathbf{H}_0|^4$ distributions of mode (6) in the *xz*-plane (cross-sectional plane of the cavity) and the *xy*-plane located 0.75 nm above the metal film (mid-point between the particle-film gap and bottom of the particle), respectively. The $|\mathbf{H}/\mathbf{H}_0|^4$ distribution of the *xz*-plane view shows that the magnetic field "hot spot" is mainly confined in the triangle region formed by the dimer and the metal film. More importantly, the induced displacement currents in the dimer and the metal film, as represented by the white cones in the *xz*-plane form a loop following the boundary of the triangular region, is the hallmark of a magnetic resonance. This feature also explains why the magnetic dipole resonance is not disclosed in the multipole expansion when the currents are only integrated in the dimer domain in Eq. (2) (see Fig. 2a), as the currents cannot form a complete loop without the contribution from the nearby gold film.

Based on these observations, we emphasize that the magnetic mode in the nanosphere DoFN has quite different resonant features to that of a nanosphere MoFN as reported before[40]. In a nanosphere MoFN with large sphere, the magnetic dipolar mode can form due to the excitation of confined displacement current loop around the gap between the particle and the film. As a result, the magnetic "hot spot" resides in the gap region between the particle and the film. The whole system of a nanosphere MoFN at the magnetic resonance behaves like a binary LC resonator whose resonance frequency is determined by the current loop circumference (proportional to the conductance L) and the gap size (inversely proportional to the capacitance C). Differently, the triangular current loop of mode (6) indicates that it comes from a ternary LC resonance where both the particle-film and the particle-particle gaps contribute to the capacitances. We find that the induced magnetic mode (6) will be suppressed if any of these capacitances is removed by shorting the corresponding gap with a metal bridge (Fig. S2). Correspondingly, the current loop of the magnetic mode (6) has quite a large circumference which intimately depends on the diameter of the nanosphere, resulting in a long resonant wavelength.

Another interesting near-field property of the magnetic mode (6) is that the "hot spots" of electric and magnetic fields are spatially separated from one another. To demonstrate this point, Fig. 3c shows the spectra of electric field enhancement factor monitored at the same locations as in Fig. 3a, where $\mathbf{E}$ and $\mathbf{E}_0$ are the total and incidence electric fields, respectively. As shown in Fig. 3b, the strongest electric field enhancement are found at the center of the particle-film gap rather than near the center of the triangular region. where the magnetic field is strongly enhanced (red line in Fig. 3a). Comparing the distributions given in Fig. 3d to those of in Fig. 3b, the separated "hot spot" regions of electric and magnetic fields are clearly visualized. This feature is also different from the magnetic resonance in a nanosphere MoFN, where both the electric and magnetic fields are enhanced in the particle-film gaps[40]. Such spatially separated electric and magnetic "hot spots" might be utilized to differentiate between the electric and magnetic enhanced photonic effects.

To experimentally observe and verify the magnetic resonances in nanosphere DoFNs as unrevealed in the above numerical results, we synthesized gold sphere dimers with ultrathin SiO_2 shells; nanosphere DoFNs were then prepared by the simple drop-casting method (see Method). A home-built polarization-resolved dark-field micro-spectroscopy system (Fig. 4a) was employed to measure the scattering responses of the samples (see Method).

We first focus on the polarized-resolved scattering responses of an exemplary nanosphere DoFN sample, the SEM image of which is given in Fig. 4a. The diameters of the gold spheres and the thickness of the SiO_2 shells of the sample are estimated to be 100 nm and 1.5 nm, respectively. Figs. 4b and 4c show the measured scattering intensities of the nanosphere DoFN in excitation configurations (I) and (II) with the incidence angle θ=70°, respectively; symbols in the figures are the original measured data points, and the

lines are the corresponding fits with multiple Lorentz functions. Note that the scattering intensity of each spectrum is normalized to its own maximum for better visualization of all scattering peaks. The measured polarization-resolved scattering spectra in Fig. 4b and 4c show excellent agreement with the numerical results (Fig. 1a and 1b). Specially, the s-polarized scattering spectrum (olive symbols and line in Fig. 4a) shows three scattering peaks at 525 nm, 653 nm, and 965 nm, respectively. Referring to the corresponding calculated spectrum (olive line) presented in Fig. 1a, we can attribute these scattering peaks to modes (4), (5), and (6) in sequence. While both modes (4) and (5) have been revealed in our previous studies, to our best knowledge it is the first experimental observation of the magnetic resonance mode (6) in a nanosphere DoFN. Similarly, all the remaining plasmon modes of the nanosphere DoFN predicted by simulation (Fig. 1a and 1b) can be visualized and distinguished from the measured polarization-resolved scattering spectra in Fig. 4b and 4c, respectively.

The slight discrepancies between the measured and calculated resonant wavelengths originate from several possible factors. Firstly, the size and morphology of the synthesized gold nanospheres are not perfectly consistent with those used in the simulation. Besides, we find that the particle-particle distance of the sample seems smaller than two times of the thicknesses of the SiO_2 shells. Also, the gold film prepared by thermal evaporation method inevitably has a certain degree of roughness (about 0.5 nm as determined by AFM measurement)[43]. Finally, we cannot exclude the impacts of possible quantum effects, most likely spatial nonlocality, considering the extremely small gaps (less than 3 nm) in the nanosphere DoFN.

Figure 4d shows the polar plot of the scattering intensity of modes (5) and (6) as a function of angle of the detection polarizer (see Method), termed here as the detection-polarization dependent scattering intensity. It is seen that both the electric mode (5) and magnetic mode (6) exhibit maximum scattering intensities when the detection polarization is parallel to the orientation of the dimer, i.e. at 0°.

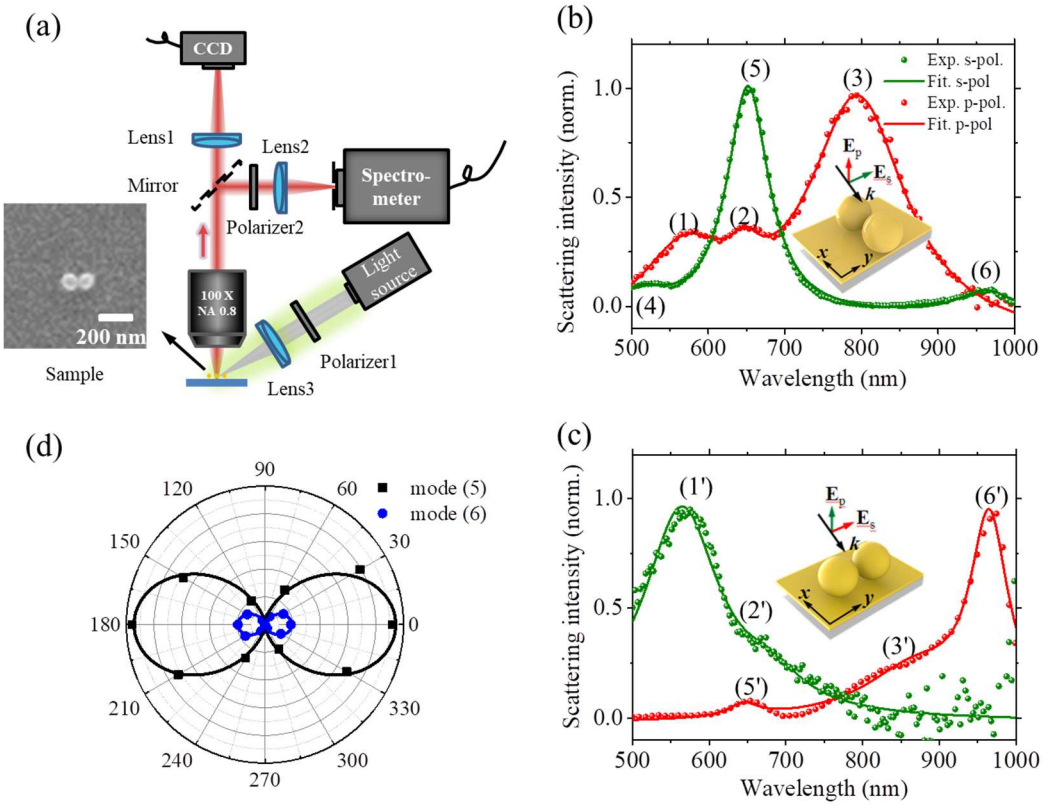

Fig. 4 Polarization-resolved dark-field scattering characterization of the nanosphere DoFN. a Schematic of the home-built polarization-resolved dark-field micro-spectroscopy system, and the SEM image of the exemplary nanosphere DoFN sample. **b** Measured s-polarized (olive line) and p-polarized (red line) scattering spectra with excitation configuration (I). **c** Similar to **b** but with excitation configuration (Ⅱ). Symbols in **b** and **c** are the measured data, and solid lines are the corresponding fits with multiple Lorentz functions. The magnitude of each data point is an intensity integral over a wavelength band of 10 nm centered at the scattering peak. **d** Polar plot of the detection-polarization dependent scattering intensity of electric mode (5) (black) and magnetic mode (6) (blue) of the nanosphere DoFN.

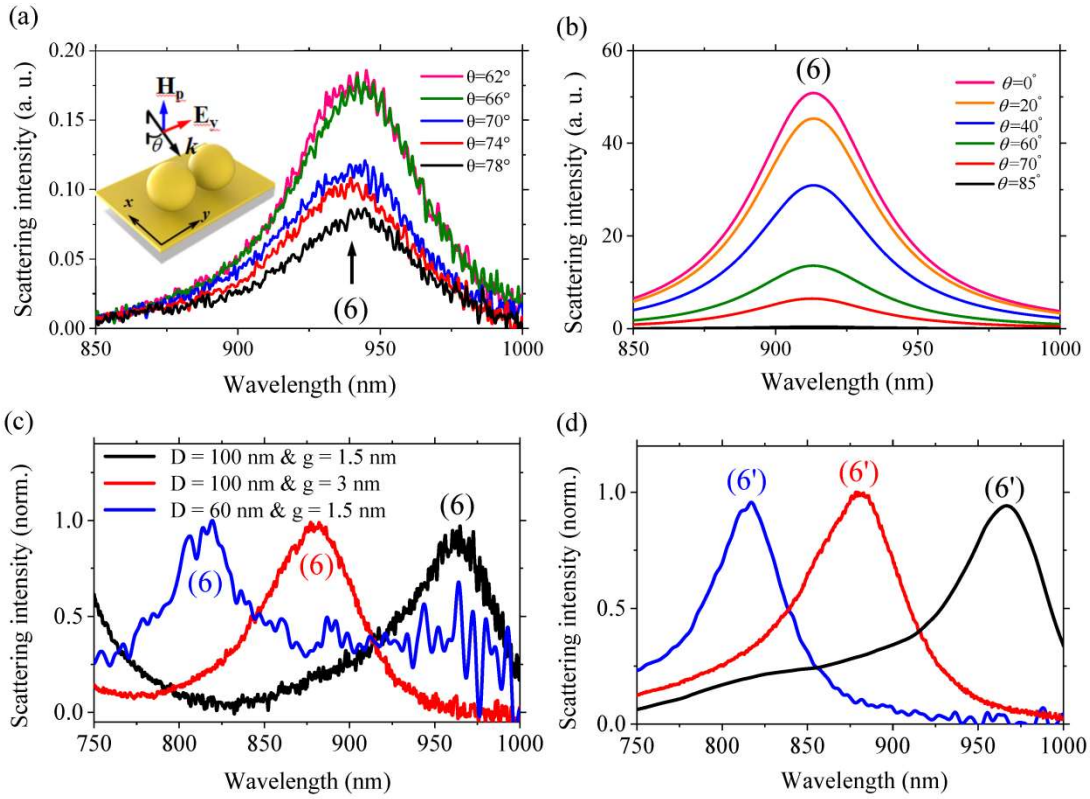

Fig. 5 Tuning the scattering intensity and resonance wavelength of the magnetic modes sustained in nanosphere DoFNs. **a** Measured s-polarized scattering spectra of the nanosphere DoFN in the excitation configuration (I), when the incidence angle θ increases from 62° to 78°. **b** Similar to **a** but the p-polarized scattering spectra in excitation configuration (II). **c** Measured s-polarized scattering spectra in excitation configuration (I) of three nanosphere DoFNs with D = 100 nm & g = 1.5 nm (black line), D = 100 nm & g = 3 nm (red line), and D =60 nm & g = 1.5 nm (blue line). **d** Measured p-polarized scattering spectra in excitation configuration (II) of the same nanosphere DoFNs in **c**. The scattering intensity of each spectrum is normalized to its own maximum

After identifying the magnetic modes from the polarization-resolved dark-field measurement, we further implement experiments to tune its resonant features. We first show that the scattering intensity of the magnetic mode (6) excited in configuration (I) can be readily modulated by adjusting the incidence angle θ (inset of Fig. 5a). To confirm this, Fig. 5a shows the measured scattering spectra of the magnetic mode (6) for different incident angles in excitation configuration (I), which shows an increasing scattering intensity as θ reduces. Limited by the optical module of our polarization-resolved dark-field spectroscopy system, the available modulating angle θ in this experiments is confined in the range between 60° to 80°. Meanwhile, the corresponding numerical results (Fig. 5b) verify that the strongest magnetic mode (6) can be excited when the plane wave is incident normally upon the dimer and the film, (i.e. θ=0°) and disappears when the incident direction is parallel to the film plane ($\theta \approx 90^{\circ}$). Intuitively, the excitation strength of the magnetic mode (6) should be proportional to the projection of the incident magnetic field on the direction across the triangular region formed by the dimer and the metal film, i.e. $|H_x|=|\mathbf{H}_p|\cos(\theta)$ according to the coordinate system given in the inset of Fig. 5a. However, more in-depth numerical investigations (Fig. S3a and S3c) indicate that the scattering intensity of mode (6) is in fact determined by the projection of the local background magnetic field at the particle position rather than the incident magnetic field. As the background field is the resultant between the incident wave and the reflected wave from the air-gold interface (see Method), it has quite a different dependence on θ than that of the incident magnetic field. Detailed numerically-calculated scattering responses of modes (5), (6), (5') and (6') as a function of the incidence angle θ are given in Fig. S3c and S3d, from which we can see how the intensities of these modes can be modulated by tuning θ.

Finally, we experimentally demonstrate that the resonant frequencies of the magnetic modes in nanosphere DoFNs can be tuned from infrared to visible range, by increasing the gap thicknesses and/or reducing the particle size. Figs. 5c and 5d

show the measured polarization-resolved scattering spectra of three nanosphere DoFN samples with different particle-film gap thicknesses (denoted as g) and diameters of the gold spheres (denoted as D). As we only concern about the variation of resonant frequency, the scattering intensity of all spectra are normalized for better visualization. Instead of synthesizing gold spheres with thicker SiO_2 shells, here we use an easier strategy by adding a dielectric (Al_2O_3) spacer between the dimer and metal film using atomic layer deposition (ALD), which allows precise control the particle-film gap size.

Comparing the scattering spectra of the samples with the same D but different g (black and red lines) in Figs. 5c and 5d, we can see that the resonant frequencies of the magnetic modes blue-shift significantly from the infrared (960 nm for the black line) to the visible range (876 nm for the blue line), when the particle-film gap size increases from 1.5 nm to 3 nm. As discussed before, the magnetic modes of the nanosphere DoFN arises from the bonding interaction between the dimer and its corresponding image in the metal film, where the coupling strength is mainly determined by g. Based on the plasmon hybridization model[34, 48], the resonant energy of a bonding mode increases when the coupling strength is mitigated by increasing g. Based on a LC resonance model, the resonant frequency of the magnetic mode is proportional to $\sqrt{1/LC}$ and can be increased when g rises, because a larger particle-film gap size reduces the capacitance C.

Alternatively, the resonant frequencies of the magnetic modes can also be tuned by changing the dimensions of the nanospheres. As an example, we show in Figs. 5c and 5d the measured polarization-resolved scattering spectrum (blue line) of a nanosphere DoFN constructed by a dimer composed of smaller gold nanospheres (D = 60 nm). The resonance frequency of the magnetic mode of this DoFN blue-shifts to about 816 nm as compared with D=100 case (black line). This observation certifies the sensitivity of the magnetic mode in the DoFN towards D, which is quite different from the magnetic resonance in a nanosphere MoFN. In a nanosphere DoFN, the dimension of the particles determines the circumference of the displacement current loop following the boundary of the triangular region formed by the dimer and the metal film (Fig. 3b). As a result, the effective coupling length between the dimer and metal film is quite sensitive to the diameter of the nanospheres, which can be utilized to tune the resonant frequency of the magnetic mode. On the contrary, the displacement current loop of the magnetic mode in a nanosphere MoFN is tightly confined around the particle-film gap. The effective particle-film coupling length (or in other words the circumference of the current loop) is mainly determined by the local morphology near the gap rather than the size of the sphere. On one hand, this characteristic implies that the nanosphere in a MoFN with small gap size must be large to provide long enough coupling length to induce a magnetic dipole mode in the visible range; On the other hand, the resonant frequency of the induced magnetic dipole mode in a MoFN is relatively insensitive towards the diameter variation of the nanosphere[40]. Based on the results in Figs. 5c and 5d, we claim that the magnetic mode in a nanosphere DoFN has a greater freedom for control that in a nanosphere MoFN.

Considering the well-established ALD technique, altering the particle-film gap size shall be the most convenient and accurate way to tune the resonant frequency of the plasmon-induced magnetic mode in a nanosphere DoFN. However, one unwilling cost of such method is the larger particle-film gap size would reduce the coupling strength, which then results in the weakening of the near-field enhancement of the mode. If we want to maintain a small gap size (less than 3 nm for example) realizing a magnetic mode in the visible range requires a reduction of the particle dimension. But as can be observed in the blue line in Fig. 5c, the signal-to-noise ratio of the measured scattering spectrum of a DoFN with small naonospheres also reduced because of the declined scattering intensity from the sample, making it more difficult to experimentally visualize the resonant modes. Therefore, in actual application, tuning the resonant frequency of the magnetic mode in a nanosphere DoFN needs simultaneous adjustment of both the gap size and particle dimension, in order to achieve a balance in the strong near-field enhancement and far-field scattering intensity.

Discussion

In conclusion, we unveiled a strong in-plane plasmon-induced magnetic dipolar mode in a DoFN constructed by a gold nanosphere dimer coupled to a gold film. Full-wave electromagnetic simulation revealed that such magnetic dipolar mode stems from the bonding interaction between electric dipoles in the dimer and induced anti-phase electric dipole in the metal film. Correspondingly, the displacement current of the structure of the mode followed a loop around a triangular region formed by the dimer and the metal film. Numerical near-field enhancement distributions indicated that the magnetic and electric near-field "hot spots" of this magnetic mode were spatially separated, with the former mainly located in the particle-film gap and the latter in the triangular region. Based on a home-built dark-field spectroscopy system, we for the first time observed experimentally the magnetic dipolar modes from the polarization-resolved scattering responses of the nanosphere DoFNs. We further demonstrated that the resonant frequency of the magnetic mode of the nanosphere DoFN can be readily tuned from infrared to visible regions by adjusting the particle-film gap thickness and the diameter of gold spheres.

Our findings of the plasmon-induced magnetic resonance in the nanosphere DoFN not only facilitate the in-depth understanding of rich plasmon modes in multiparticle-on-film nanocavities, but also promise many photonic applications relying on optical artificial magnetism, such as optical metamaterials, absorbing metasurfaces, nonlinear spectroscopy, and magnetic plasmonic devices. In addition, nanosphere DoFNs provide an excellent platform for exploring plasmon magnetic resonance-enhanced spectroscopies, such as surface-enhanced Raman spectroscopy and plasmon-exciton strong-coupling effects by inserting two dimensional materials into the particle-film gaps as a spacer. We also expect that the magnetic resonances in nanosphere DoFNs to exhibit more interesting interactions with other electric modes (for example Fano resonance) when the symmetry of the cavity is broken, e.g. by using a heterodimer composed of non-identical particles.

Materials and methods

Preparation and SEM Characterization of Nanosphere DoFN Samples

A 100 nm-thick gold film was prepared on an ultra-clean coverslip (Schott Nexterion, Germany) using a thermal evaporator (Nexdep, Angstrom Engineering, Inc.). Gold nanospheres of diameters 100 nm and 60 nm were purchased from NanoSeeds, Inc., Hong Kong. All the purchased gold nanospheres were covered with 1 nm thick cetyltrimethylammonium bromide (CTAB) layers. Then the CTAB layers of gold nanospheres were cleaned off and replaced by ~1.5 nm thick SiO_2 shells based on an advanced chemical synthesizing method[49]. Finally, the rinsed and water-diluted monodisperse gold nanospheres were drop-cast on the gold film and left to dry in air for seconds to form particle-on-film nanocavities. SEM characterization of the samples was performed with a JEOL JSM-6335F.

Polarization-Resolved Dark-Field Spectroscopy

Optical scattering spectroscopy at the single particle-particle level was carried out with a home-built polarization-resolved dark-field micro-spectroscopy system. The whole system was based on an Olympus BX51 upright microscope equipped with a $100\times$ dark-field objective (LMPlan, Olympus, NA=0.8), a spectrometer (Acton SP2300, Princeton Instruments), a grey CCD camera (PIXIS:400BR eXcelon, Princeton Instruments), an external white-light source, and other optical path and polarization adjusting elements (see experimental setups in Figure 3a).

Oblique incident white-light coming from the external light source was collimated and focused on the samples. The polarization direction of the incident wave was modulated by a polarizer inserted in the excitation path. Scattered light was collected through a dark-field objective and directed to the spectrometer and CCD to get the scattering spectra and dark-field images.

The orientations of the dimers in the samples were obtained by our previously developed polarization-resolved nanometrology spectroscopy method[43]. In short, the samples were firstly illuminated by the unpolarized white-light from a built-in light source of the microscope, and the observed dark-field images will alter between green and red colors when a polarizer inserted in the detection path is rotated. The long axis of the

dimer can determined by the angle of the detection-polarizer when the red scattering intensity reaches the strongest.

Numerical Simulations

Full-wave electromagnetic simulations were performed by COMSOL Multiphysics V5.2 based on finite element method (FEM). Permittivity of gold was taken from the empirical data given by Johnson and Christy[50]. Considering the metal film of the fabricated samples is optically thick, a semi-infinite thick gold substrate was adopted in the simulation. The structure was excited by a predefined background field obtained by using Fresnel formulas for a gold-air interface, which contains the incident and reflected waves above the interface and transmitted wave below. The whole computation domain was surrounded by a perfect matched layer (PML) to eliminate unwanted reflections at the boundaries. Scattering spectra of the nanocavities were obtained by collecting the upward scattering power flow in a solid angle of 103°, corresponding to NA = 0.8 of the collection objective used in the experiments. The meshes of the simulation models, especially in the domain closely enclosing the dimer, were deliberately refined to confirm the convergence of the computation.

Acknowledgements

We acknowledge the financial support by the Hong Kong Research Grants Council (GRF Grant No. 15303417), the National Natural Science Foundation of China (Grant No. 11474240 and 21861132016), the China Postdoctoral Science Foundation (2018M630356), and the Hong Kong Polytechnic University (Grant No. G-SB82).

Author contributions

#Y.M., Q.Z. and D.Y.L contributed equally to this work. Q.Z. performed numerical simulations and multipolar expansion calculations. D.Y.L. and Q.Z. conceived the idea and designed the research. Y.M. prepared silica-coated gold nanosphere dimers on a gold thin film and performed dark-field scattering spectroscopy and SEM imaging. Y.L., W.X. and S.L. synthesized the silica-coated gold nanospheres. Q.Z. and D.Y.L. wrote the manuscript based on a brief research summary by Y.M. All authors contributed to the interpretation of the results and the revision of the manuscript, and have given approval to the submission of this work.

Conflict of interest

The authors declare no competing financial interest.

Supplementary information is available for this paper at DOI: xxx…

ORCID

Dangyuan Lei: 0000-0002-8963-0193

Wei Xie: 0000-0002-8290-514X

References

1. Smith, D. R., Pendry, J. B., Wiltshire, M. C. K. Metamaterials and negative refractive index. *Science* **305**, 788-792 (2004).
2. Shalaev, V. M. Optical negative-index metamaterials. *Nat. Photonics* **1**, 41-48 (2007).
3. Dolling, G. et al. Low-loss negative-index metamaterial at telecommunication wavelengths. *Opt. Lett.* **31**, 1800-1802 (2006).
4. Chen, H.-T., Taylor, A. J., Yu. N. A review of metasurfaces: physics and applications. *Rep. Prog. Phys.* **79**, 076401 (2016).
5. Vaskin, A. et al. Manipulation of magnetic dipole emission from Eu^{3+} with Mie-resonant dielectric metasurfaces. *Nano Lett*. **19**, 1015-1022 (2019).
6. Campione, S., Guclu, C., Ragan, R., Capolino, F. Enhanced magnetic and electric fields via Fano resonances in metasurfaces of circular clusters of plasmonic nanoparticles. *ACS Photonics* **1**, 254-260 (2014).
7. Pendry, J. B., Holden, A. J., Robbins, D. J., Stewart, W. J. Magnetism from conductors and enhanced nonlinear phenomena. *IEEE Tran. Microwave Tech.* **47**, 2075-2084 (1999).
8. Aydin, K. et al. Investigation of magnetic resonances for different split-ring resonator parameters and designs. *New J. Phys.* **7**, 168-168 (2005).
9. Rockstuhl, C. et al. On the reinterpretation of resonances in split-ring-resonators at normal incidence. *Opt. Express* **14**, 8827-8836 (2006).
10. Zhou, J. et al. Saturation of the magnetic response of split-ring resonators at optical frequencies. *Phys. Rev. Lett.* **95**, 223902 (2005).
11. Sarychev, A. K., Shvets, G., Shalaev, V. M. Magnetic plasmon resonance. *Phys. Rev. E* **73**, 036609 (2006).
12. Monticone, F., Alù, A. The quest for optical magnetism: from split-ring resonators to plasmonic nanoparticles and nanoclusters. *J. Mater. Chem. C* **2**, 9059-9072 (2014).
13. Calandrini, E. et al. Magnetic hot-spot generation at optical frequencies: from plasmonic metamolecules to all-dielectric nanoclusters. *Nanophotonics* **8**, 45-62 (2018).
14. Tribelsky, M. I. et al. Small dielectric spheres with high refractive index as new multifunctional elements for optical devices. *Sci. Rep.* **5**, 12288 (2015).
15. Kivshar, Y., Miroshnichenko, A. Meta-optics with Mie resonances. *Opt. Photon. News* **28**, 24-31 (2017).
16. Kuznetsov, A. I. et al. Optically resonant dielectric nanostructures. *Science* **354**, aag2472 (2016).
17. Schuller, J. A., Zia, R., Taubner, T., Brongersma, M. L. Dielectric metamaterials based on electric and magnetic resonances of silicon carbide particles. *Phys. Rev. Lett.* **99**, 107401 (2007).
18. Maier, S. A. *Plasmonics: Fundamentals and Applications* (Springer, New York, 2007).
19. Novotny, L., Hecht, B., Keller, O. *Principles of Nano-Optics* (Cambridge Univ. Press, 2006).

20. Fan, J. A. et al. Self-assembled plasmonic nanoparticle clusters. *Science* **328**, 1135-1138 (2010).
21. Shafiei, F. et al. A subwavelength plasmonic metamolecule exhibiting magnetic-based optical Fano resonance. *Nat. Nanotechnol.* **8**, 95-99 (2013).
22. Sheikholeslami, S. N., Garcia-Etxarri, A., Dionne, J. A. Controlling the interplay of electric and magnetic modes via Fano-like plasmon resonances. *Nano Lett.* **11**, 3927-3934 (2011).
23. Roller, E. M. et al. DNA-assembled nanoparticle rings exhibit electric and magnetic resonances at visible frequencies. *Nano Lett.* **15**, 1368-1373 (2015).
24. Nazir, A. et al. Fano coil-type resonance for magnetic hot-spot generation. *Nano Lett.* **14**, 3166-3171 (2014) .
25. Liu, N. et al. Magnetic plasmon formation and propagation in artificial aromatic molecules. *Nano Lett.* **12**, 364-369 (2012).
26. Hentschel, M. et al. Transition from isolated to collective modes in plasmonic oligomers. *Nano Lett.* **10**, 2721-2726 (2010).
27. Liu, N. et al. Manipulating magnetic plasmon propagation in metallic nanocluster networks. *ACS Nano* **6**, 5482-5488 (2012).
28. Montoni, N. P., Quillin, S. C., Cherqui, C., Masiello, D. J. Tunable Spectral Ordering of Magnetic Plasmon Resonances in Noble Metal Nanoclusters. *ACS Photonics* **5**, 3272-3281 (2018).
29. Lorente-Crespo, M. et al. Magnetic hot spots in closely spaced thick gold nanorings. *Nano Lett.* **13**, 2654-2661 (2013).
30. Liu, N. et al. Infrared perfect absorber and its application as plasmonic sensor. *Nano Lett.* **10**, 2342-2348 (2010).
31. Moreau, A. et al. Controlled-reflectance surfaces with film-coupled colloidal nanoantennas. *Nature* **492**, 86-89 (2012).
32. Akselrod, G. M. et al. Large-area metasurface perfect absorbers from visible to near-infrared. *Adv. Mater.* **27**, 8028-8034 (2015).
33. Liu, Y. et al. Compact magnetic antennas for directional excitation of surface plasmons. *Nano Lett.* **12**, 4853-4858 (2012).
34. Nordlander, P., Prodan, E. Plasmon hybridization in nanoparticles near metallic surfaces. *Nano Lett.* **4**, 2209-2213 (2004).
35. Zhang, Q., Li, G. C., Lo, T. W., Lei, D. Y. Polarization-resolved optical response of plasmonic particle-on-film nanocavities. *J. Opt.* **20**, 024010 (2018).
36. Li, G. C., Zhang, Q., Maier, S. A., Lei, D. Plasmonic particle-on-film nanocavities: a versatile platform for plasmon-enhanced spectroscopy and photochemistry. *Nanophotonics* **7**, 1865-1889 (2018).
37. Mertens, J. et al. How light is emitted by plasmonic metals? *Nano Lett.* **17**, 2568-2574 (2017).
38. Mertens, J. et al. Controlling subnanometer gaps in plasmonic dimers using graphene. *Nano Lett.* **13**, 5033-5038 (2013).
39. Mock, J. J. et al. Distance-dependent plasmon resonant coupling between a gold nanoparticle and gold film. *Nano Lett.* **8**, 2245-2252 (2008).
40. Chen, S. et al. Plasmon-induced magnetic resonance enhanced Raman spectroscopy. *Nano Lett.* **18**, 2209-2216 (2018).
41. Huang, Y. et al. Hybridized plasmon modes and near-field enhancement of metallic nanoparticle-dimer on a mirror. *Sci. Rep.* **6**, 30011 (2016).
42. Chen, S. et al. How to light special hot spots in multiparticle-film configurations? *ACS Nano* **10**, 581-587 (2016).
43. Li, G. C., Zhang, Y. L., Lei, D. Y. Hybrid plasmonic gap modes in metal film-coupled dimers and their physical origins revealed by polarization resolved dark field spectroscopy. *Nanoscale* 8, 7119-7126 (2016).
44. Li, G. C., Zhang, Y. L., Jiang, J., Luo, Y., Lei, D. Y. Metal-substrate-mediated plasmon hybridization in a nanoparticle dimer for photoluminescence line-width shrinking and intensity enhancement. *ACS Nano* **11**, 3067-3080 (2017).
45. Terekhov, P. D. et al. Multipolar response of nonspherical silicon nanoparticles in the visible and near-infrared spectral ranges. *Phys. Rev. B* **96**, 035443 (2017).
46. Liu, W., Zhang, J., Lei, B., Hu H. Toroidal dipole-induced transparency in core–shell nanoparticles. *Laser Photonics Rev.* **9**, 564-570 (2015).
47. Zhang, Q. et al. Exploring optical resonances of nanoparticles excited by optical Skyrmion lattices. *Opt. Express* **27**, 7009-7022 (2019).
48. Nordlander, P. et al. Plasmon hybridization in nanoparitlce dimers. *Nano Lett.* **4**, 899-903 (2004).
49. Xie, W., Walkenfort, B., Schlücker, S. Label-free SERS monitoring of chemical reactions catalyzed by small gold nanoparticles using 3D plasmonic superstructures. *J. Am. Chem. Soc.* **135**, 1657-1660 (2013).
50. Johnson, P. B., Christy, R. W. Optical constants of the Noble metals. *Phys. Rev. B* **6**, 4370-4379 (1972).